Chapter 4

Free Vibration Analysis of an Inflated Torus

4.1 Introduction

As mentioned in the first chapter, an inflated torus is used as a structural support system in many inflatable structures (antenna, entry and landing system, etc.) and it is the focus of this study. Because of the very thin wall, the inflated torus can be modeled using shell theory. In the second chapter, we presented the governing equations for static and dynamic analysis of a shell under pressure. These equations will be solved in this chapter for free vibration analysis of an inflated torus of circular cross-section.

From Fig. 1.1, one can observe that while the inner rim of the torus is attached to a mirror, the outer rim is free. Ignoring the effect of the mirror, we take the boundary condition of the torus to be free. It is assumed that the cross-section of the torus remains circular after the static deformation and the pressure remains constant after the static deformation and

during vibration. We assume the wall thickness to be uniform and the material to be elastic and isotropic. While we do consider the internal pressure, other effects of enclosed gas are ignored. The torus considered in this study is complete, i.e. has no edges.

First, the toroidal shell geometry is presented and the initial stresses due to internal pressure are obtained. Thereafter, solution of the dynamic equations of motion is attempted. These equations are essentially three coupled partial differential equations and hence difficult to solve exactly. To circumvent this problem, we use Galerkin's method. First, the displacement functions are written in a separation of variable form. The displacement function in the longitudinal direction is written in terms of complete waves of sines and cosines. This reduces the governing equations to ordinary differential equations with variable coefficients. Then, the displacement function in the meridional direction is represented using Fourier series and written in two separate groups to demonstrate the independent symmetric and antisymmetric modes of vibration. We also describe the procedure to derive the standard eigenvalue problem, which provides the natural frequencies and mode shapes. In numerical analysis, first, a circular cylinder without pressure (a special case of the torus with pressure) is considered. Thereafter, the inflated torus is considered. In both cases, the results are compared with published ones. A detailed analysis of mode shapes and natural frequencies is presented for the inflated torus. Thereafter, a parametric study is conducted in order to study the effects of aspect ratio (ratio of the two radii), pressure, and thickness on the natural frequencies and mode shapes. The above results are obtained using an accurate geometric nonlinearity with the follower action of the pressure force. In the past, several researchers used simplified equations and ignored the direct pressure force. Also, analysis using a commercial finite element code generally ignores the direct pressure effect and considers only prestresses. Using numerical results, we show that these simplifications lead to inaccurate natural frequencies and mode shapes. After that, we compare the results with experiments and conclude the chapter.

4.2 Geometry of a Toroidal Shell

The middle surface of the toroidal shell is generated by the revolution of a circle of radius r with its center at a distance R ($=\frac{1}{\kappa}$) from the axis of revolution (Fig. 4.1). Instead of using the general shell coordinate notations α_1 and α_2, we use ϕ and s for the toroidal shell. Let ϕ and s be the curvilinear coordinates in the meridional and longitudinal directions, respectively, and let ζ be the radial direction. The Lamé parameters A_ϕ and A_s and the principal radii of curvatures R_ϕ and R_s are as follows (Plaut et al., 2000):

$$A_\phi = r, \qquad A_s = 1 + r\kappa\cos\phi \tag{4.1}$$

$$R_\phi = r, \qquad R_s = r + \frac{1}{\kappa\cos\phi} \tag{4.2}$$

The Lamé parameters and the radii of curvature given by Eqs. (4.1) and (4.2) define the geometrical shape of a toroidal shell. These quantities are substituted in the equations derived in the second chapter in order to obtain the specialized equations for a toroidal shell.

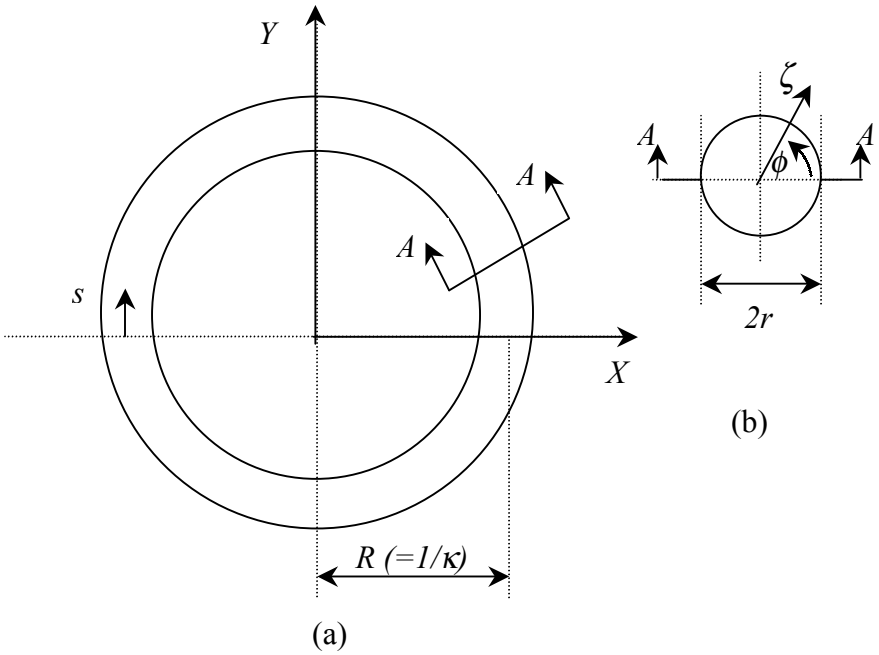

Fig. 4.1: Geometry of the torus: (a) side view; (b) section A-A.

4.3 Initial Stress Resultants

The in-plane stress resultants N_{ϕ}^{r}, N_{s}^{r}, and $N_{\phi s}^{r}$ associated with the constant internal pressure can be obtained by solving the three static equations presented in the first chapter (Eqs. 2.96). Since the toroidal shell and the loading due to the internal pressure are axisymmetric, Eqs. (2.96) can also be written in axisymmetric form. In order to solve the static equations, we observe that due to this axisymmetric property $N_{\phi s}^{r} = 0$ and $\frac{\partial(\cdot)}{\partial s} = 0$. In addition, the stress resultants should be continuous along the tube. Using these conditions, the following expressions for the stress resultants can be obtained for a torus of constant circular cross-section (Plaut et al., 2000):

$$N_{\phi}^{r} = \frac{pr}{2}\frac{(2 + r\kappa\cos\phi)}{(1 + r\kappa\cos\phi)}, \qquad N_{s}^{r} = \frac{pr}{2}, \qquad N_{\phi s}^{r} = 0 \tag{4.3}$$

These initial in-plane stress resultants (N_{ϕ}^{r}, N_{s}^{r}, and $N_{\phi s}^{r}$) due to the internal pressure (p) are also called prestresses and will be used in the governing equations.

4.4 Solution Procedure

For the free vibration problem, we drop the external loading terms in the governing Eqs. (2.98). The governing equations in terms of the displacement fields can be written in the following short forms:

$$l_{11}\{u_{\phi}\} + l_{12}\{u_{s}\} + l_{13}\{w\} - A_{\phi}A_{s}\rho h\ddot{u}_{\phi} = 0, \tag{4.4}$$

$$l_{21}\{u_{\phi}\} + l_{22}\{u_{s}\} + l_{23}\{w\} - A_{\phi}A_{s}\rho h\ddot{u}_{s} = 0, \tag{4.5}$$

$$l_{31}\{u_\phi\} + l_{32}\{u_s\} + l_{33}\{w\} - A_\phi A_s \rho h \ddot{w} = 0\,, \tag{4.6}$$

where l_{ij} ($i, j = 1, 2, 3$) are the linear differential operators. For harmonic vibration we can eliminate the time dependence by writing

$$u_\phi(\phi,s,t) = U(\phi,s)e^{i\omega t}\,, \qquad u_s(\phi,s,t) = V(\phi,s)e^{i\omega t}\,, \qquad w(\phi,s,t) = W(\phi,s)e^{i\omega t}\,. \tag{4.7}$$

where ω is the natural frequency. The torus considered in this study, is complete i.e., has no edges, and has free boundary conditions. This implies that the displacement functions and their derivatives need to satisfy the continuity condition and they should be periodic. Let's assume that the displacement functions (U, V, W) can be separated spatially in the following forms:

$$U(\phi,s) = U_\phi(\phi)U_s(s)\,, \qquad V(\phi,s) = V_\phi(\phi)V_s(s)\,, \qquad W(\phi,s) = W_\phi(\phi)W_s(s)\,. \tag{4.8}$$

Now, the equilibrium equations can be reduced to a set of ordinary differential equations if the motion is assumed to be composed of complete waves in the form of sine and cosine functions in the longitudinal direction. To this end, we replace the displacement functions $U_s(s)$, $V_s(s)$, and $W_s(s)$ in Eq. (4.8) by either

$$U_s(s) = \sin\left(\frac{ns}{R}\right), \qquad V_s(s) = -\cos\left(\frac{ns}{R}\right), \qquad W_s(s) = \sin\left(\frac{ns}{R}\right), \tag{4.9}$$

or,

$$U_s(s) = \cos\left(\frac{ns}{R}\right), \qquad V_s(s) = \sin\left(\frac{ns}{R}\right), \qquad W_s(s) = \cos\left(\frac{ns}{R}\right). \tag{4.10}$$

Here n, called the wave number, is an integer and $n \neq 0$. In fact, when $n \neq 0$, substitution of Eqs. (27) or (28) will yield the same natural frequencies but two independent mode shapes

related to each other by a rotation. The modes of the same frequency but different orientation arise because of the symmetry of the torus, and the rotation is such that the pair of modes, Eqs. (4.9) and (4.10), are orthogonal to each other (Fig. 4.2). For $n = 0$, Eqs. (4.9) and (4.10) will yield different natural frequencies. Mode shapes corresponding to $n = 0$ in Eqs. (4.9) and (4.10) are called axisymmetric modes. The mode shapes corresponding to Eq. (4.9) and $n = 0$ are also called dilationless circumferential modes or purely torsional modes.

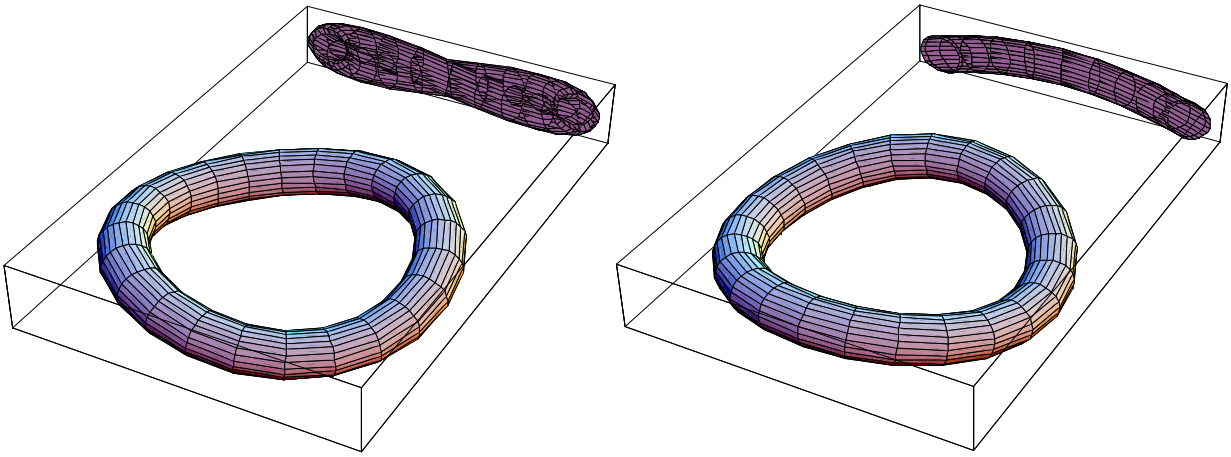

Fig. 4.2: An orthogonal pair of non-axisymmetric modes.

After the above substitutions, we divide Eqs. (4.4), (4.5), and (4.6) by $U_s(s)$, $V_s(s)$, and $W_s(s)$, respectively, to eliminate s-dependency. Now we can write Eqs. (4.4) - (4.6) as

$$l_{11\phi}\{U_\phi(\phi)\} + l_{12\phi}\{V_\phi(\phi)\} + l_{13\phi}\{W_\phi(\phi)\} + A_\phi A_s \rho h \omega^2 U_\phi(\phi) = 0 \tag{4.11}$$

$$l_{21\phi}\{U_\phi(\phi)\} + l_{22\phi}\{V_\phi(\phi)\} + l_{23\phi}\{W_\phi(\phi)\} + A_\phi A_s \rho h \omega^2 V_\phi(\phi) = 0 \tag{4.12}$$

$$l_{31\phi}\{U_\phi(\phi)\} + l_{32\phi}\{V_\phi(\phi)\} + l_{33\phi}\{W_\phi(\phi)\} + A_\phi A_s \rho h \omega^2 W_\phi(\phi) = 0 \tag{4.13}$$

where $l_{ij\phi}$ $(i, j = 1, 2, 3)$ can be derived from l_{ij} using the above procedure. The resulting Eqs. (4.11) - (4.13) are the linear differential equations with variable coefficients in ϕ and can

be solved using Galerkin's method (Soedel, 1986; Leung and Kwok, 1994). We can write the resulting equations in the following matrix form:

$$\boldsymbol{L}_\phi \, \boldsymbol{\Phi} + \lambda \, \boldsymbol{m} \, \boldsymbol{\Phi} = 0 \tag{4.14}$$

where $\lambda = \omega^2$ and $\boldsymbol{L}_\phi$ is a matrix of the differential operators in ϕ. The matrices $\boldsymbol{L}_\phi$ and $\boldsymbol{m}$ and the displacement vector $\boldsymbol{\Phi}$ are given by

$$\boldsymbol{L}_\phi = \begin{bmatrix} l_{11\phi} & l_{12\phi} & l_{13\phi} \\ l_{21\phi} & l_{22\phi} & l_{23\phi} \\ l_{31\phi} & l_{32\phi} & l_{33\phi} \end{bmatrix}, \quad \boldsymbol{m} = \begin{bmatrix} A_\phi A_S \rho h & 0 & 0 \\ 0 & A_\phi A_S \rho h & 0 \\ 0 & 0 & A_\phi A_S \rho h \end{bmatrix}, \quad \boldsymbol{\Phi} = \begin{Bmatrix} U_\phi(\phi) \\ V_\phi(\phi) \\ W_\phi(\phi) \end{Bmatrix} \tag{4.15}$$

We consider the integral statement of the system of differential equations

$$\int_\Omega [\boldsymbol{\Phi}_a{}^T \boldsymbol{L}_\phi \, \boldsymbol{\Phi} + \lambda \, \boldsymbol{\Phi}_a{}^T \boldsymbol{m} \, \boldsymbol{\Phi}] \, d\Omega = 0 \tag{4.16}$$

where Ω is the domain in which the system of differential equations is to be satisfied, $\boldsymbol{\Phi}_a$ is an arbitrary weighting function vector, and the superscript T denotes the transpose of a matrix. Choosing the arbitrary weighting function $\boldsymbol{\Phi}_a$ as a variation of $\boldsymbol{\Phi}$, denoted by $\boldsymbol{\delta\Phi}$, we get

$$\int_0^{2\pi} [\boldsymbol{\delta\Phi}^T \boldsymbol{L}_\phi \, \boldsymbol{\Phi} + \lambda \, \boldsymbol{\delta\Phi}^T \boldsymbol{m} \, \boldsymbol{\Phi}] \, d\phi = 0 \tag{4.17}$$

McGill (1966) showed that the deflection function of a torus could be made up of solutions such that either

a) $V(\phi, s)$ and $W(\phi, s)$ are even and $U(\phi, s)$ is odd with respect to $\phi = 0$ and π, or

b) $V(\phi, s)$ and $W(\phi, s)$ are odd and $U(\phi, s)$ is even with respect to $\phi = 0$ and π.

The modes of type (a) are called symmetric modes, because they yield a symmetric picture of a meridional cross-section with respect to $\phi = 0$ and π (Fig. 4.3-a). Similarly, mode shapes of type (b) are known as antisymmetric modes because of the antisymmetric pattern with respect to $\phi = 0$ and π (Fig. 4.3-b).

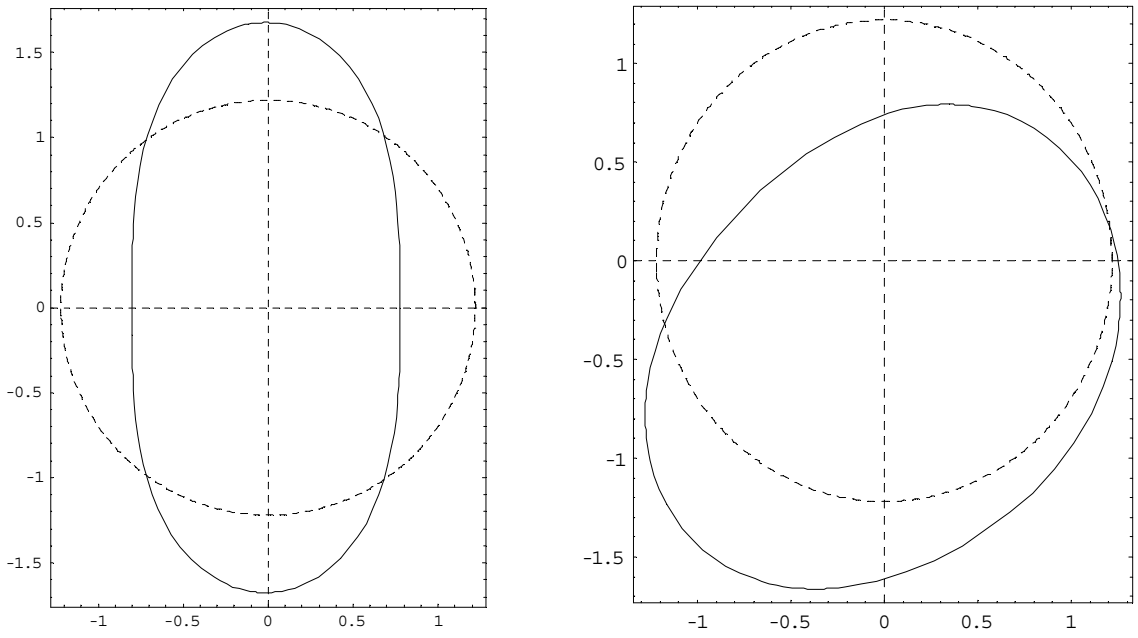

(a) Symmetric deformation (b) Antisymmetric deformation

Fig. 4.3: Symmetrically and antisymmetrically deformed cross-sections of the torus. Solid lines are the deformed cross-sections and dotted lines are the undeformed cross-sections and axes.

Therefore, the symmetric and antisymmetric groups of vibration modes can be analyzed independently. It is also evident that the displacement function must be a continuous periodic function with continuous periodic derivatives of the same period in ϕ. Hence $U_\phi(\phi)$, $V_\phi(\phi)$, and $W_\phi(\phi)$ can be represented by Fourier series. Taking a finite number of terms (*m)* in the Fourier series, we can write the symmetric part, denoted by superscript *s*, as

$$U_\phi^s(\phi) = \sum_{i=1}^{m} A_i^s \sin(i\phi) \qquad V^s{}_\phi(\phi) = \sum_{i=0}^{m-1} B_i{}^s \cos(i\phi) \qquad W_\phi^s(\phi) = \sum_{i=0}^{m-1} C_i^s \cos(i\phi)\,. \quad (4.18)$$

Similarly, we can write the antisymmetric part as

$$U_\phi^a(\phi) = \sum_{i=0}^{m-1} A_i^a \cos(i\phi) \qquad V_\phi^a(\phi) = \sum_{i=1}^{m} B_i^a \sin(i\phi) \qquad W_\phi^a(\phi) = \sum_{i=1}^{m} C_i^a \sin(i\phi) \tag{4.19}$$

where superscript *a* denotes the antisymmetric part. Thus the vector $\boldsymbol{\Phi}$ can be written as

$$\boldsymbol{\Phi} = \boldsymbol{f}\ \boldsymbol{a} \tag{4.20}$$

where $\boldsymbol{a}$ is the vector of unknown coefficients A_i^s, B_i^s, and C_i^s in the symmetric case, and A_i^a, B_i^a, and C_i^a in the antisymmetric case (i =1, 2,...m), and $\boldsymbol{f}$ is a matrix so that $\boldsymbol{f}\,\boldsymbol{a}$ gives the displacement vector $\boldsymbol{\Phi}$ in Eq. (4.20). Now we can write Eq. (4.17) as

$$\int_0^{2\pi} [\delta \boldsymbol{a}^T \boldsymbol{f}^T \boldsymbol{L}\, \boldsymbol{f}\, \boldsymbol{a} + \lambda\, \delta \boldsymbol{a}^T \boldsymbol{f}^T \boldsymbol{m}\, \boldsymbol{f}\, \boldsymbol{a}]\, d\phi = \boldsymbol{0} \tag{4.21}$$

Since $\boldsymbol{\delta a}$ is arbitrary, we have

$$\int_0^{2\pi} [\boldsymbol{f}^T \boldsymbol{L}\, \boldsymbol{f}\, \boldsymbol{a} + \lambda\, \boldsymbol{f}^T \boldsymbol{m}\, \boldsymbol{f}\, \boldsymbol{a}]\, d\phi = \boldsymbol{0} \tag{4.22}$$

The above equation after integration can be written in the following matrix form:

$$(\boldsymbol{A} + \lambda\, \boldsymbol{B})\, \boldsymbol{a} = \boldsymbol{0} \tag{4.23}$$

where the matrices $\boldsymbol{A}$ and $\boldsymbol{B}$ are given by

$$\boldsymbol{A} = \int_0^{2\pi} \boldsymbol{f}^T \boldsymbol{L}\, \boldsymbol{f}\, d\phi\,, \qquad \boldsymbol{B} = \int_0^{2\pi} \boldsymbol{f}^T \boldsymbol{m}\, \boldsymbol{f}\, d\phi\,. \tag{4.24}$$

Equation (4.23) is an eigenvalue problem. The eigenvalue λ corresponds to the natural frequencies, and the eigenvector $\boldsymbol{a}$ corresponds to the vibration mode shapes.

4.5 Vibration of a Cylindrical Shell

First, we consider a special case of torus where the radius R of the torus (Fig. 4.1-a) becomes very large compared to the radius r of the cross-section of the torus so that the geometry of the toroidal shell becomes close to that of a circular cylinder. For this special case, we also assume that the internal pressure (p) is zero (Table 4.1). The results are compared with the exact natural frequencies (Leissa, 1973). The shear diaphragm boundary condition has been assumed. The length of the cylinder is taken to be πR so that the boundary conditions are satisfied exactly by the displacement function in the longitudinal direction (Eq. (4.9)).

Table 4.1: Data for the geometry and material of the cylinder.

Parameter	**Values**
Elastic modulus (E), Pa	$2.07\mu 10^{11}$
Thickness (h), m	0.01
Poisson's ratio (ν)	0.3
Density (ρ), Kg/m^3	7800
Length (L), m	7.62
Radius of the cross-section (r), m	1.219

Table 4.2 shows the natural frequencies calculated using this analysis and the exact solution. Since the exact solution was also obtained using Sanders' linear theory, the results show perfect agreement. In this case, the symmetric and antisymmetric vibrations give the same natural frequencies. This is because a circular cylinder possesses symmetry in the meridional direction and hence the symmetric and antisymmetric modes are related to each other simply by a rotation. However, some vibration modes, e.g., torsional vibration modes,

can only be predicted by antisymmetric modes. Since every term in the displacement function (Eqs. (4.18) and (4.19)) constitutes a mode shape for a circular cylinder, the convergence is independent of the number of terms taken in the series.

Table 4.2: Comparison of natural frequencies for the cylinder.

Mode number	Axial wave number, circumferential wave number (n, i)	Frequency from this analysis (Hz)	Exact values (Hz) (Leissa, 1973)
1	1, 2	5.91	5.91
2	1, 1	11.76	11.76
3	1, 3	12.83	12.83
4	2, 3	14.67	14.67
5	2, 2	15.65	15.65
6	3, 3	20.52	20.52
7	1, 4	24.35	24.35

4.6 Vibration of an Inflated Toroidal Shell

4.6.1 Rigid-Body Modes

The boundary of the inflated torus is considered free and hence there are six rigid-body modes corresponding to six zero natural frequencies. Out of the six rigid-body motions, three are translations and the other three are the rotations about the three perpendicular axes (Fig. 4.4). It is worth noting here that one of the main advantages of using Sanders' shell theory is that, unlike Love's shell theory, strains do vanish for all six small rigid-body motions. The following displacement functions give rise to the rigid-body modes (Kordes, 1960):

a) Displacement parallel to the axis of symmetry, V_Z :

$$U(\phi,s) = A\cos(\phi), \qquad V(\phi,s) = 0, \qquad W(\phi,s) = A\sin(\phi) \tag{4.25}$$

b) Displacement perpendicular to the axis of symmetry, V_X and V_Y:

$$U(\phi,s) = A\sin(\phi)\sin(s/R), \quad V(\phi,s) = -A\cos(s/R), \quad W(\phi,s) = -A\cos(\phi)\sin(s/R)$$

$$U(\phi,s) = A\sin(\phi)\cos(s/R), \quad V(\phi,s) = A\sin(s/R), \quad W(\phi,s) = -A\cos(\phi)\cos(s/R) \tag{4.26}$$

c) Rotation about the axis of symmetry, Ω_Z:

$$U(\phi,s) = 0, \qquad V(\phi,s) = A\{R + r\cos(\phi)\}, \qquad W(\phi,s) = 0 \tag{4.27}$$

d) Rotation about axes perpendicular to the axis of symmetry, Ω_X and Ω_Y:

$$U(\phi,s) = A\{r + R\cos(\phi)\}\sin(\frac{s}{R}), \; V(\phi,s) = -Ar\sin(\phi)\cos(\frac{s}{R}), \quad W(\phi,s) = AR\sin(\phi)\sin(\frac{s}{R})$$

$$U(\phi,s) = A\{r + R\cos(\phi)\}\cos(\frac{s}{R}), \; V(\phi,s) = Ar\sin(\phi)\sin(\frac{s}{R}), \quad W(\phi,s) = AR\sin(\phi)\cos(\frac{s}{R}) \tag{4.28}$$

where V_X, V_Y, and V_z are the displacement of the torus along the coordinates X, Y, and Z, respectively. Similarly, Ω_X, Ω_Y, and Ω_z are the rotations of the torus along the coordinates X, Y, and Z, respectively. Using the above rigid-body modes, the zero natural frequencies were verified.

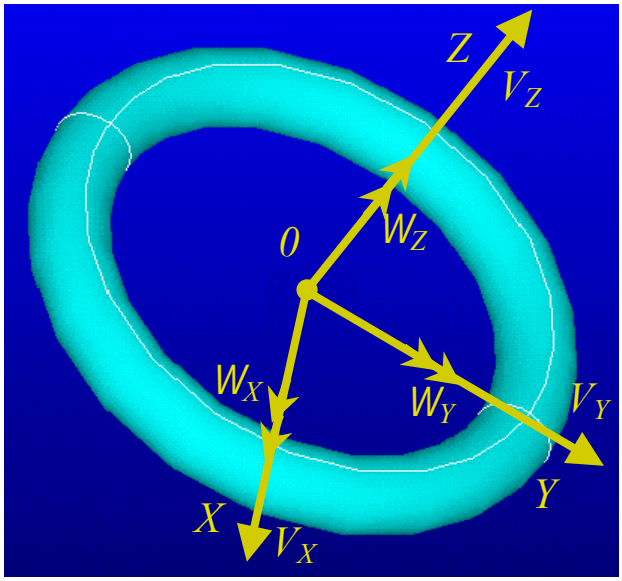

Fig. 4.4: Directions of displacements and rotations of the rigid-body-modes

4.6.2 Non-Rigid-Body Modes

In this section, we present the non-rigid-body modes and corresponding natural frequencies of an inflated torus. First, we compare the natural frequencies with those given in Liepins (1965). The results will be shown in terms of the following nondimensional quantities:

$$\eta = \frac{r}{R}, \qquad \zeta = \frac{p\,r}{E\,h}, \qquad \mu = \frac{\rho\, r^2}{E\eta^2}\omega^2 \tag{4.29}$$

where η, ζ, and μ denote the aspect ratio, prestress parameter, and frequency parameter, respectively. Table 4.3 shows the values for these parameters, symmetry, and wave number. The natural frequency shown corresponds to the first mode in each case. The results match closely. The small differences may be because Liepins (1965) used a finite difference method, while we used Galerkin's method with Fourier series.

Table 4.3: Comparison of natural frequencies of the inflated torus ($\eta = 0.3, \zeta = 0.002$).

Wave number (n), Symmetry (First mode)	Frequency parameter (μ) from this analysis	Frequency parameter (μ) from Liepins (1965)
0, symmetric	0.40	0.39
0, antisymmetric	0.04	0.04
1, symmetric	0.39	0.38
1, antisymmetric	0.23	0.23
2, symmetric	0.05	0.05
2, antisymmetric	0.04	0.04

A candidate for the material of an inflatable structure is Kapton®. Since an inflatable structure is the main interest of this work, we use this material for the analysis. The internal pressure has been taken to be 0.5 psi as it is the desired internal pressure for inflatable satellites (Tinker, 1998). Table 4.4 shows the data for the geometry and material of the inflatable torus.

Table 4.4: Data for the geometry and material of the torus.

Parameter	**Values**
Elastic modulus (E), N/m^2	$2.55\mu 10^9$
Wall-thickness (h), m	$76.2\mu 10^{-6}$
Poisson's ratio (ν)	0.34
Density (ρ), Kg/m^3	1418
Radius of torus (R), m	7.62
Radius of the cross-section (r), m	1.22
Internal pressure (p), N/m^2	3447.38

The first natural frequencies and mode shapes with their projections on one plane are shown in Figs. 4.5. Modes 1, 3, 4, 6, 8, 10, and 12 are of antisymmetric type. Out of these modes, 1, 3, 8, and 12 are the out-of-plane bending modes. These modes resemble the

bending modes of a free-free beam, as can be seen from their projections. The rest of the modes are of symmetric type. In mode 2, the torus vibrates by forming an elliptical shape. Similarly, in modes 5 and 9, it forms triangular and square shapes, respectively. These modes bend in the plane of the torus and hence they are called in-plane bending modes. Modes 4 and 7 are the axisymmetric modes. In an axisymmetric mode, the shape does not change along the *s*-direction, but the cross-section deforms either antisymmetrically, called the axisymmetric antisymmetric mode (mode 4), or symmetrically, called the axisymmetric symmetric mode (mode 7). Note that, except for axisymmetric modes, all the modes come in orthogonal pairs. In Fig. 4.5, we have shown only one of these pairs. Other modes of the pair can be obtained by a rotation. For the wave number *n*, the two mode shapes will be related to each other by a rotation of $\pi/(2n)$. It can be observed that for the same non-zero wave number (*n*), symmetric and antisymmetric modes have close frequencies. For example, symmetric and antisymmetric modes for $n = 2$ have the frequencies *6.90* Hz and *7.24* Hz, respectively. Similarly, *17.71* Hz and *18.55* Hz are the two frequencies corresponding to $n = 3$. This also brings the point that frequencies for different wave number are relatively more separated (*6.90* Hz and *7.24* Hz at $n = 2$ vs. *17.71* Hz and *18.55* Hz at $n = 3$). Another important comment on this line is that, in general, natural frequencies of the inflated torus occur in clusters and there are several modes near a particular frequency. For instance, including the repeated modes due to the symmetry in circumferential direction, there are more than *20* modes between *43* and *46* Hz. The closeness of frequencies is less evident at lower end, e.g., there are four frequencies between *6* Hz and *8* Hz. As we will see in Chapter 6, these close frequencies necessitate consideration of a high number of modes in the vibration control problem so as to reduce the spillover effect. Following a similar procedure, one can also calculate the natural frequencies and mode shapes of a torus without internal pressure by putting all the pressure related terms to zero in the equations of motion.

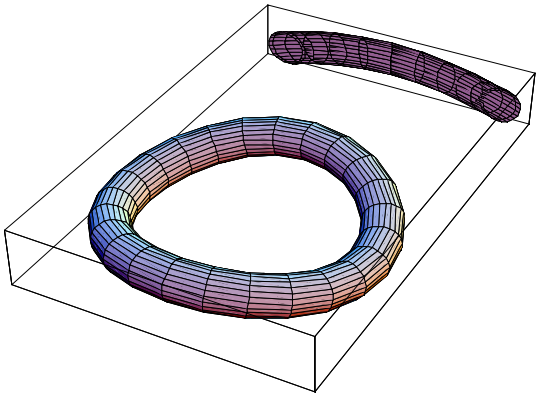

Mode 1 (6.90 Hz), n = 2
1st out-of-plane bending mode

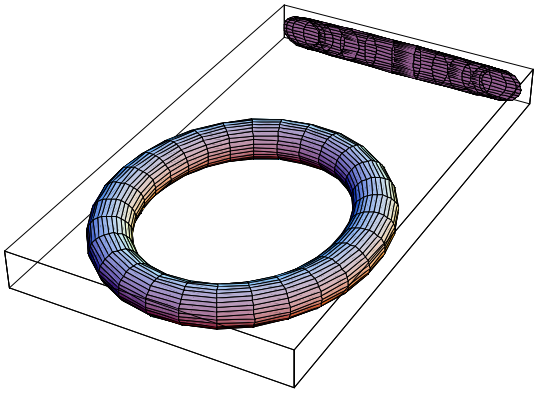

Mode 2 (7.24 Hz), n = 2
1st in-plane bending mode

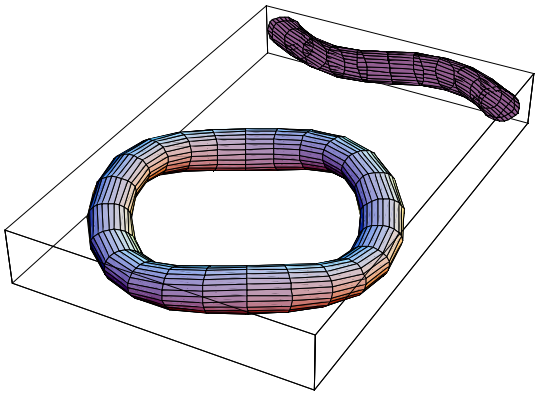

Mode 3 (17.71 Hz), n = 3
2nd out-of-plane bending mode

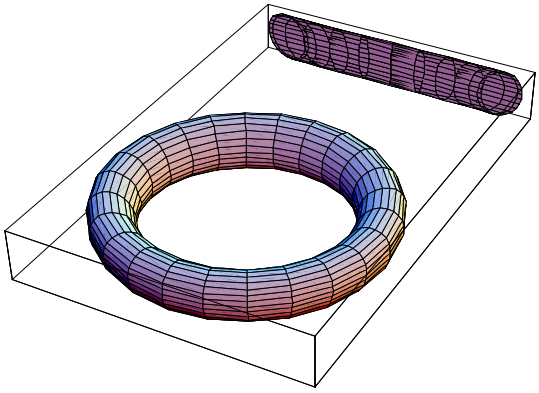

Mode 4 (17.85 Hz), n = 0
1st axisymmetric mode (antisymmetric)

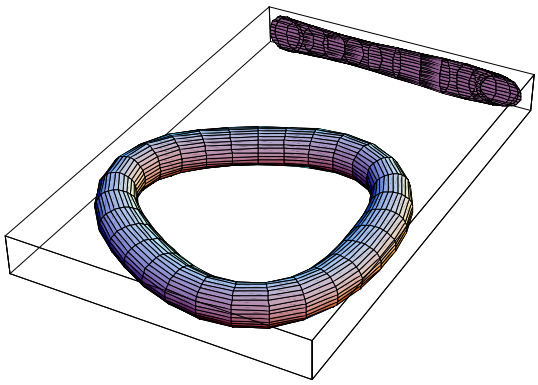

Mode 5 (18.55 Hz), n = 3
2nd in-plane bending mode

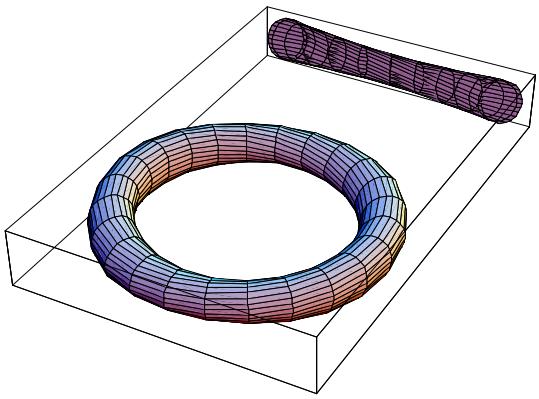

Mode 6 (24.85 Hz), n = 1
3rd antisymmetric mode (twisting)

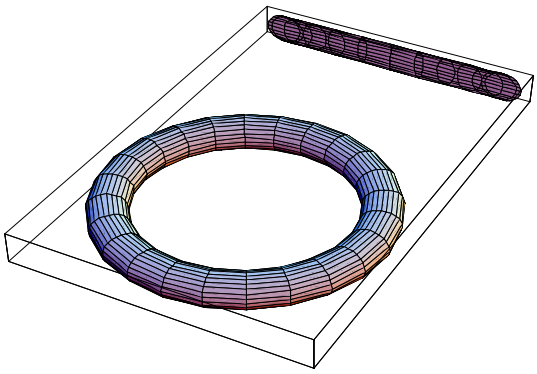

Mode 7 (28.45 Hz), n = 0
2nd axisymmetric mode (symmetric)

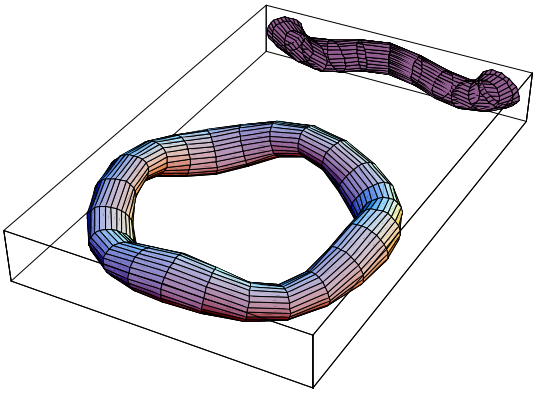

Mode 8 (30.33 Hz), n = 4
3rd out-of-plane bending mode

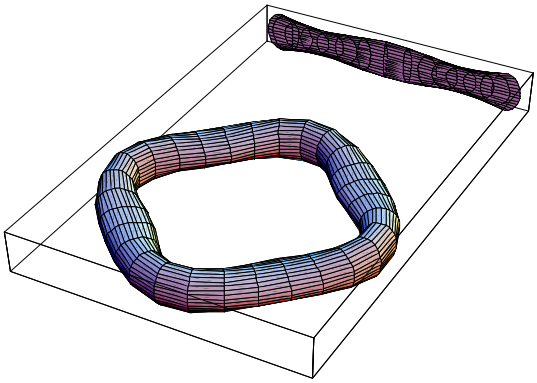

Mode 9 (31.61 Hz), n = 4
3rd in-plane bending mode

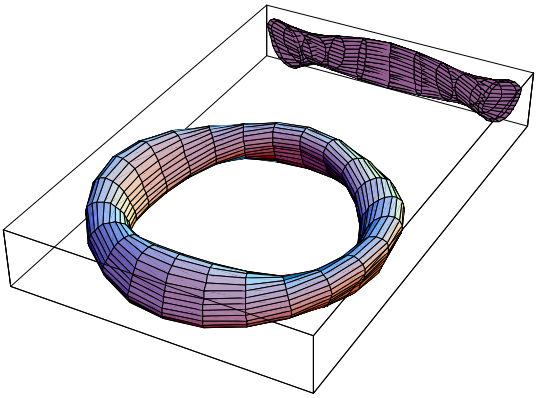

Mode 10 (38.53 Hz), n = 2
5th antisymmetric mode

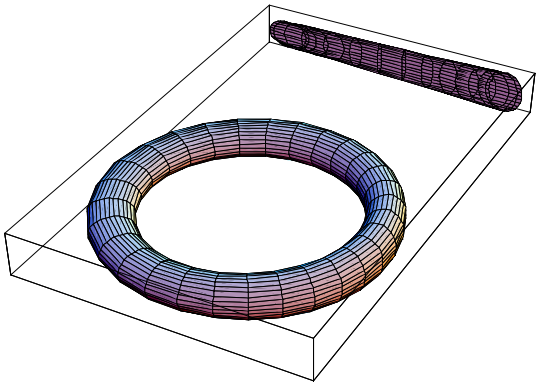

Mode 11 (38.81 Hz), n =1
4th symmetric mode

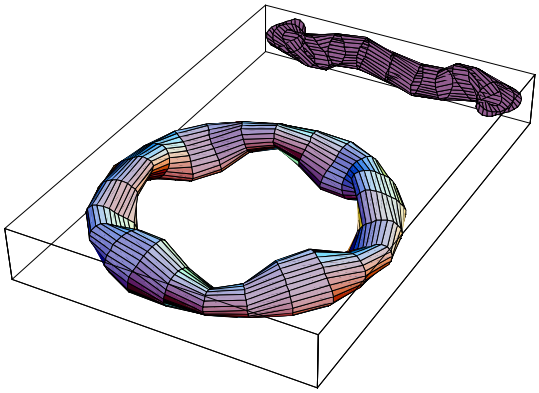

Mode 12 (42.96 Hz), n = 4
5th out-of-plane bending mode

Fig. 4.5: Mode shapes of the inflated torus.

4.6.3 Parametric Study

Now we consider the effects of aspect ratio (r/R), internal pressure (p), and wall-thickness (h) on the natural frequencies and mode shapes of the inflated torus. Parameters will be changed from the values given in Table 4.4 and the effects will be noted. Unless mentioned otherwise, values given in Table 4.4 are used.

4.6.3.1 Aspect Ratio

To study the effect of the aspect ratio, we consider frequencies at a low wave number ($n = 0$) and at a high wave number ($n = 4$). Figure 4.6 shows the natural frequencies as the aspect ratio (r/R) of the torus changes when $n = 0$. As the aspect ratio increases, frequencies decrease. It can be seen that the rate of decrease is very high up to the aspect ratio of approximately *0.1*. Comparing to the frequencies at a low aspect ratio, we see that the frequencies are more closely spaced at a high aspect ratio. Figure 4.7 shows the plot of the natural frequencies against the aspect ratio for $n = 4$. Unlike the frequencies for $n = 0$, we see that the first frequencies of both the symmetric and the antisymmetric mode increase up to an aspect ratio of around *0.26*. Again, at low aspect ratio, the frequencies are wide apart, contrary to the behavior at high aspect ratio. Similar behaviors were noticed at the internal pressure of *0.25* psi.

Table 4.5 compares the first ten mode shapes of an inflated torus at low and high aspect ratios. We see that the complexity of mode shapes increases with the increase in aspect ratio. For a low aspect ratio torus, the ring types of modes (in-plane and out-of-plane bending modes) dominate the lower modes. On the other hand, for the torus of high aspect ratio, the local deformation of the meridional curve (cross-section) dominates even in the lower modes. For example, while the first six modes of the torus at the aspect ratio of *0.06* are composed of three in-plane bending modes and three out-of-plane bending modes, the first six modes of the torus of aspect ratio *0.26* are composed of axisymmetric modes as well as twisting-type modes. The aspect ratio of a torus also influences the wave numbers of modes. Wave number relates to the periodicity of the shape around the circumference and

there could be several modes at a particular wave number in both symmetric and antisymmetric cases. In this regard, it should be noted that, at low aspect ratio, each mode has different wave number and symmetry in lower modes. On the other hand, at high aspect ratio, more than one mode of the same wave number and symmetry occurs. For example, modes *2* and *8* at the aspect ratio of *0.26* are symmetric and both correspond to the wave number *2*. This is the reason why at the high aspect ratio the wave number is less than *3* for the first ten modes, while it is up to *5* for the low aspect ratio. Mode shapes play important roles in determining the performance of actuators and sensors, and these effects will be explored in chapter 5.

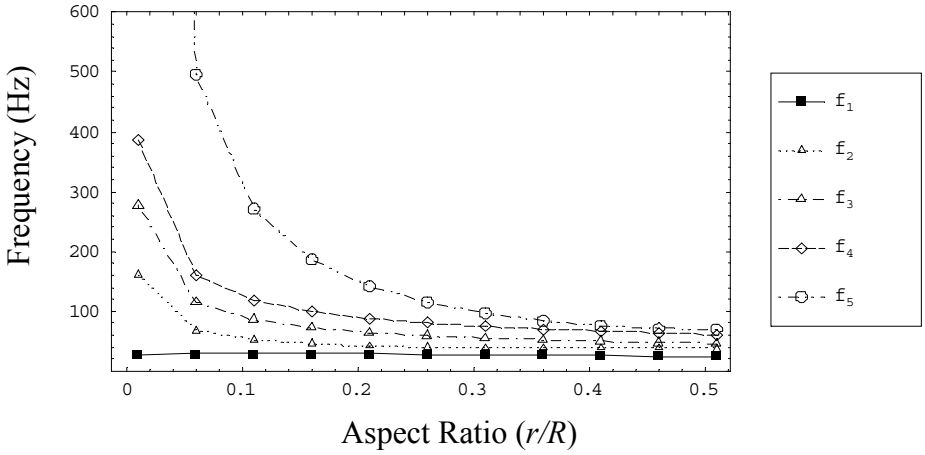

(a) Frequencies of symmetric modes for $n = 0$

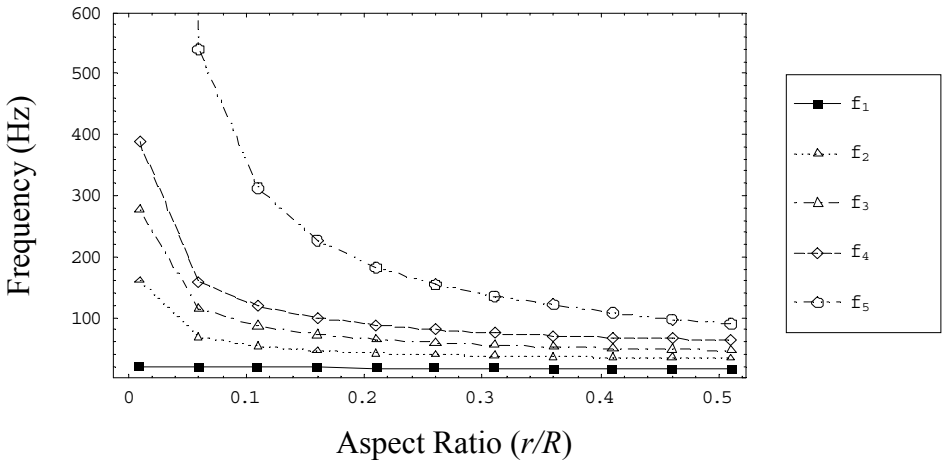

(b) Frequencies of antisymmetric modes for $n = 0$

Fig. 4.6: The first five natural frequencies vs. the aspect ratio of (a) symmetric modes and (b) antisymmetric modes corresponding to $n = 0$.

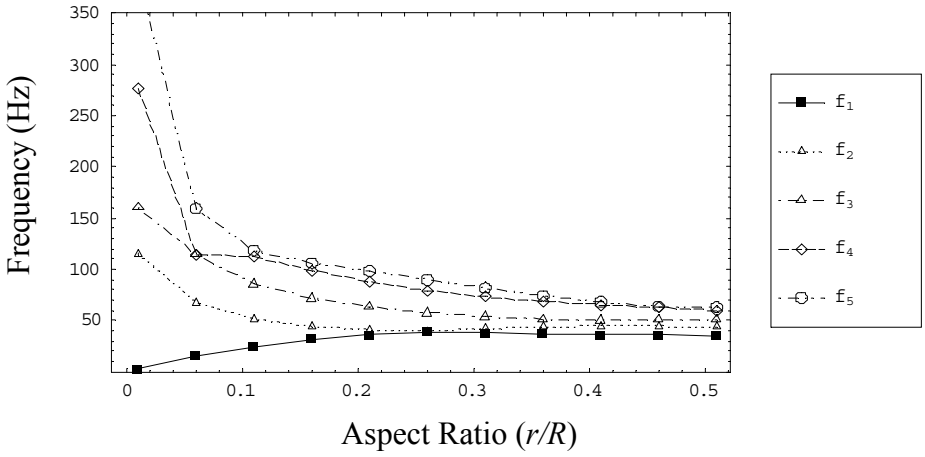

(a) Frequencies of symmetric modes for $n = 4$

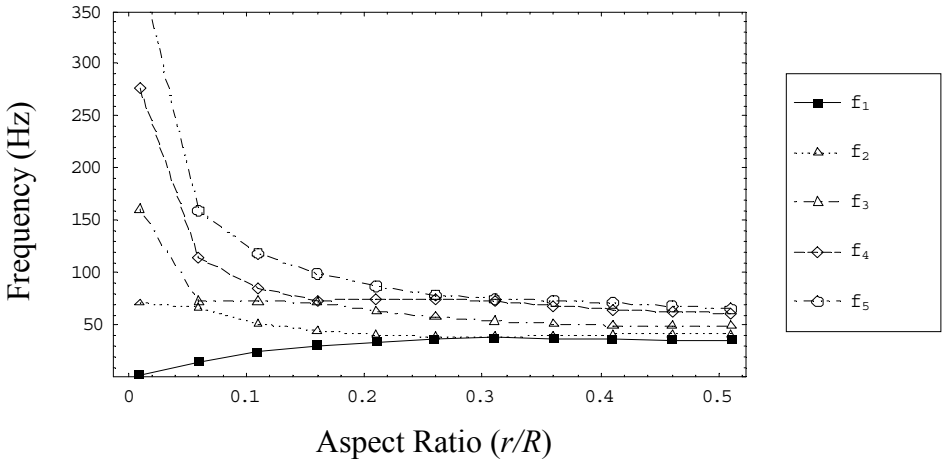

(b) Frequencies of antisymmetric modes for $n = 4$

Fig. 4.7: The first five natural frequencies vs. the aspect ratio of (a) symmetric modes and (b) antisymmetric modes corresponding to $n = 4$.

Table 4.5: Mode shapes of the inflated torus at low and high aspect ratio

Mode Number	Low aspect ratio (0.06)	High aspect ratio (0.26)
1	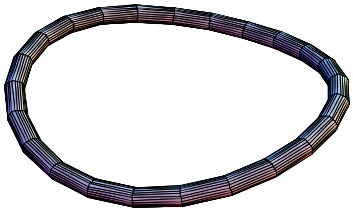 2.95 Hz, n = 2, Antisymmetric	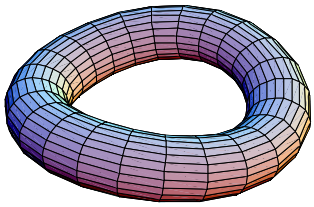 9.59 Hz, n = 2, Antisymmetric
2	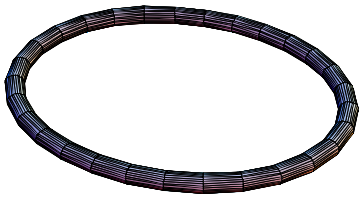 3.03 Hz, n = 2, Symmetric	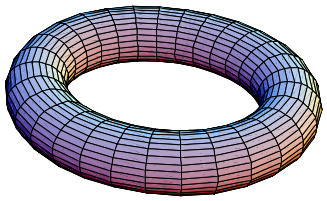 10.47 Hz, n = 2, Symmetric
3	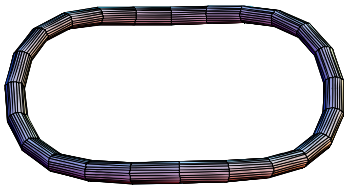 8.25 Hz, n = 3, Antisymmetric	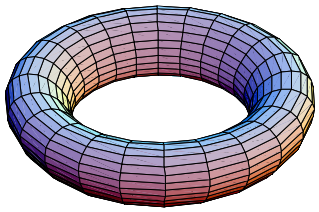 16.78 Hz, n = 0, Antisymmetric
4	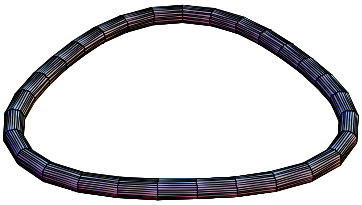 8.41 Hz, n = 3, Symmetric	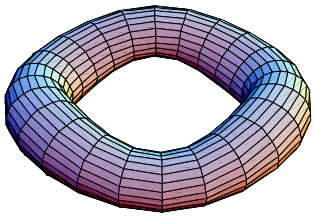 22.84 Hz, n = 3, Antisymmetric
5	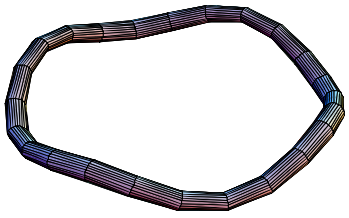 15.45 Hz, n = 4, Antisymmetric	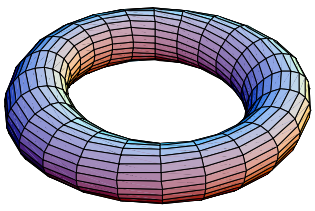 24.59 Hz, n = 1, Antisymmetric

6	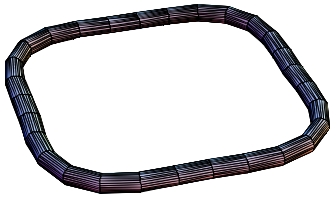 15.67 Hz, n = 4, Symmetric	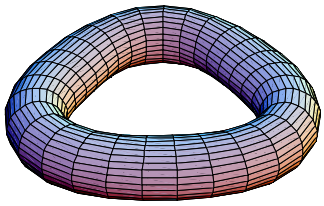 24.88 Hz, n = 3, Symmetric
7	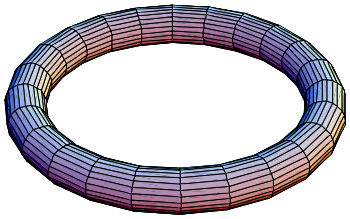 19.06 Hz, n = 0, Antisymmetric	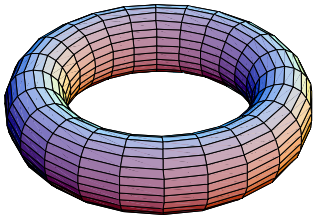 28.04 Hz, n = 0, Symmetric
8	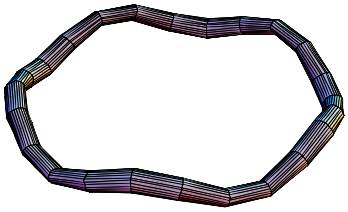 24.18 Hz, n = 5, Antisymmetric	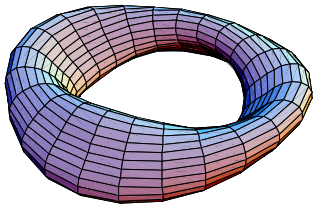 34.14 Hz, n = 2, Antisymmetric
9	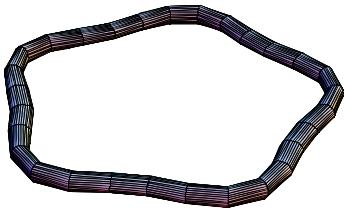 24.47 Hz, n = 5, Symmetric	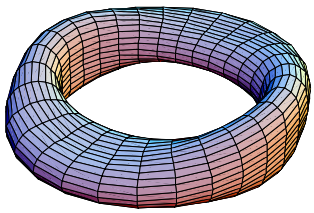 34.32 Hz, n = 2, Symmetric
10	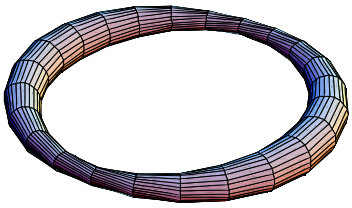 25.64 Hz, n = 1, Antisymmetric	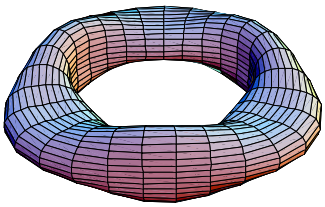 35.17 Hz, n = 3, Symmetric

4.6.3.2 Pressure

The aspect ratio of the torus is fixed once it is in space. However, the same is not true about the internal pressure. As the satellite rotates, it encounters orbital eclipse and orbital day, which bring changes in the temperature of the internal gas. This change in temperature, in turn, causes a change in internal pressure (Tinker, 1998). Hence, it is important to know how the change in internal pressure affects the natural frequencies and mode shapes of an inflated torus. Figure 4.8 shows the effect of pressure on the natural frequencies. In an inflatable structure, the major source of stiffness is the internal pressure. Hence, as the internal pressure increases, the effective stiffness of the torus increases. This causes an increase in the frequencies with the internal pressure (Fig. 4.8). The rate of increase in the frequencies is not constant throughout the pressure range. First the natural frequencies increase rapidly, and thereafter they increase slowly or remain nearly constant.

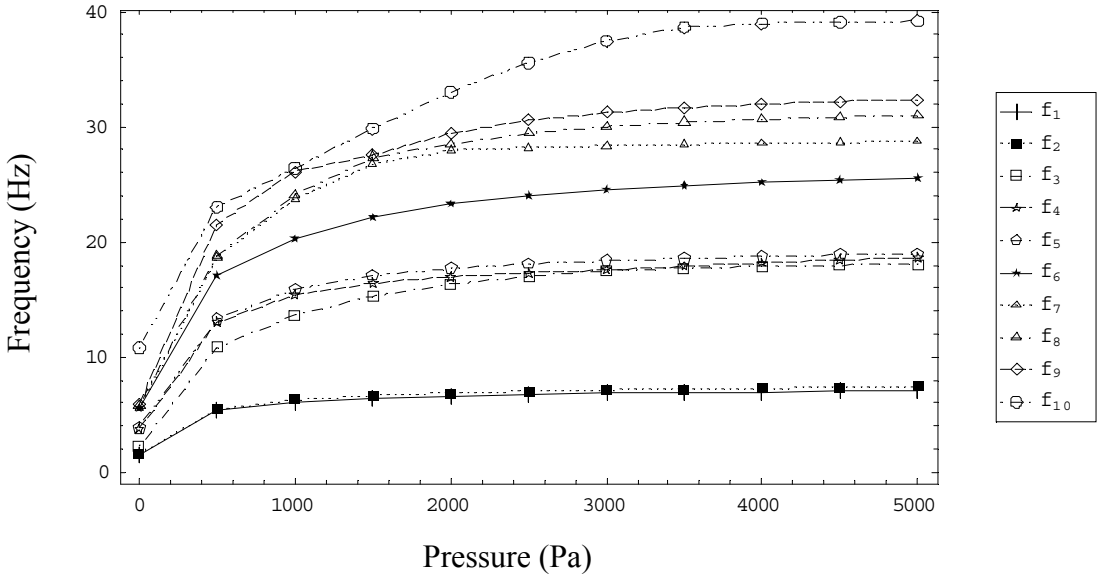

Fig. 4.8: Effect of the internal pressure on the first ten natural frequencies.

The change in pressure brings two main effects on the mode shapes. First, the order of mode shapes changes, e.g., the axisymmetric antisymmetric mode occurs at the third place at 0.25 psi and the same mode occurs at the fourth place at 0.75 psi. Another important effect occurs due to the change in stiffness. At a lower pressure, the torus undergoes higher local deformation of its surface, again because of the lower effective stiffness. This is demonstrated in Fig. 4.9, where we plot the 3rd in-plane bending mode shape at internal pressures of 0.25 psi and 0.75 psi. At 0.25 psi, we see that the cross-sectional bulge is more prominent.

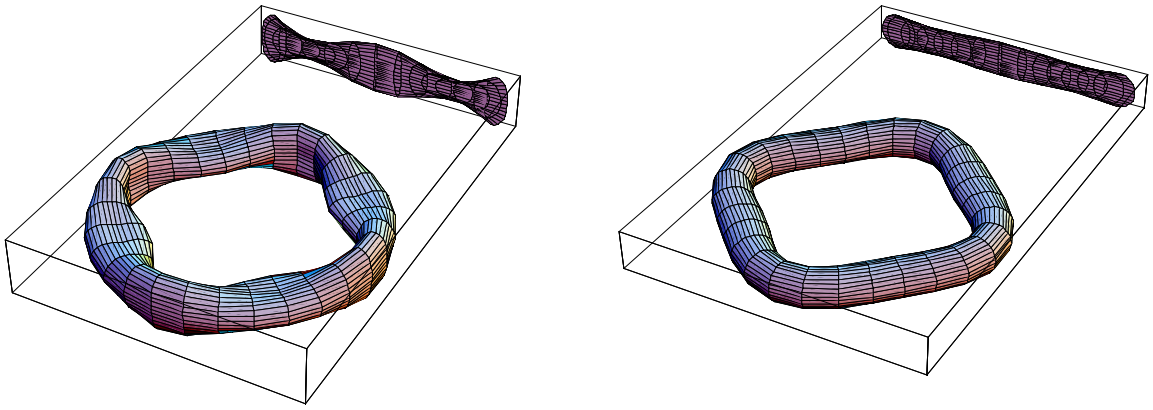

Mode 9 (28.42 Hz), p = 0.25 psi
3rd in-plane bending mode

Mode 9 (32.43 Hz), p = 0.75 psi
3rd in-plane bending mode

Fig. 4.9: Effect of the internal pressure on a mode shape

4.6.3.3 Wall-Thickness

Figure 4.10 shows how the natural frequencies change with the wall-thickness of the torus. Initially the frequency decreases fast and later it decreases slowly. The wall-thickness changes both the stiffness and the mass of the torus. While the former increases the frequency, the later effect reduces it. When the thickness is low, the stiffness is mostly due to the internal pressure and hence the mass effect is more prominent and hence the frequency of the torus decreases. Conversely, at higher thickness, the effect of pressure is less, and

stiffness and mass effects counterbalance. This keeps the frequencies almost constant after a thickness of around 5 mm. The figure suggests that a torus with a thicker wall will have very closely-spaced natural frequencies. Vibration testing and control of such a torus would be more difficult compared to a torus with smaller wall-thickness. The effect of an increase in wall-thickness on the mode shapes is also noteworthy. Not only does it change the mode characteristics (symmetry, wave number), but also the deformation is quite different for the same characteristics. An example of this phenomenon is shown in Fig 4.11, which shows the first bending and twisting modes of tori with small wall-thickness (*76.2* mm) and high wall-thickness (*5* mm). The figure shows local shape changes in the thick-wall torus as opposed to mostly global deformation in the thin-wall torus. Local surface deformation becomes even more prominent in the higher modes of the thick-wall torus.

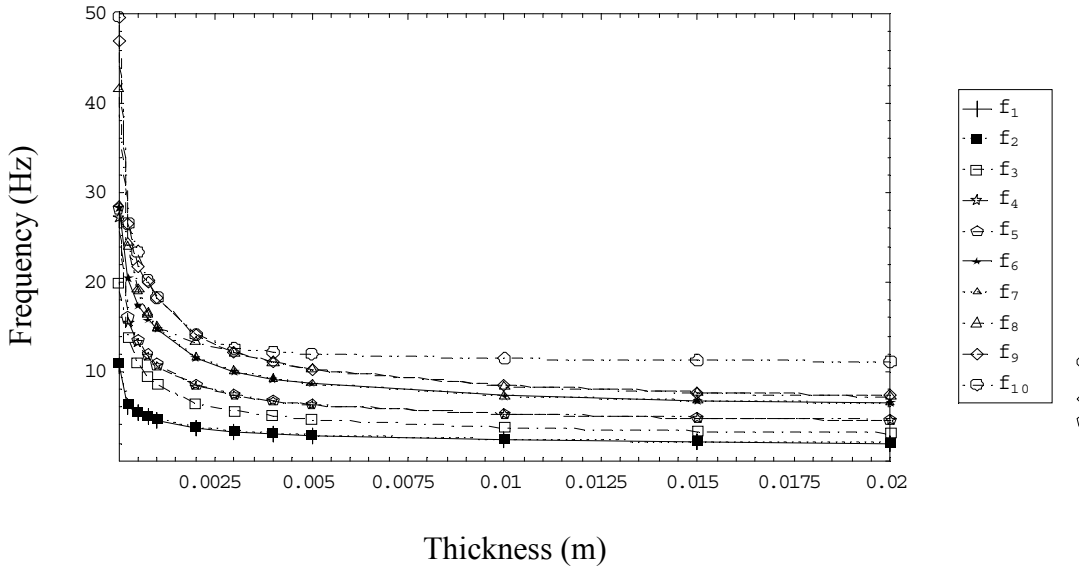

Fig. 4.10: Effect of the thickness on the natural frequencies of the inflated torus.

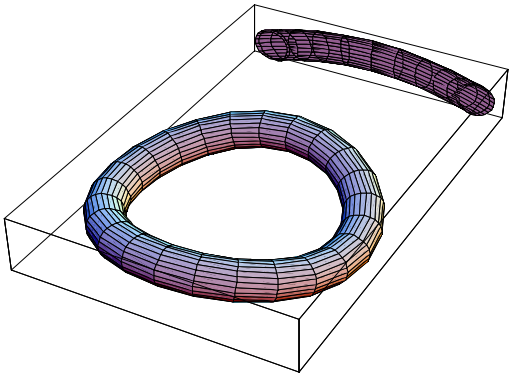

Mode 1 (6.90 Hz), h = 76.2 mm
1st out-of-plane bending mode

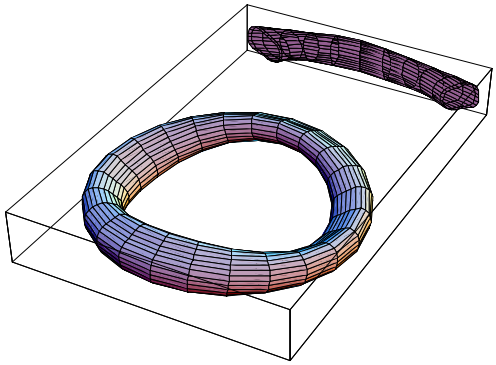

Mode 2 (2.90 Hz), h = 5 mm
1st out-of-plane bending mode

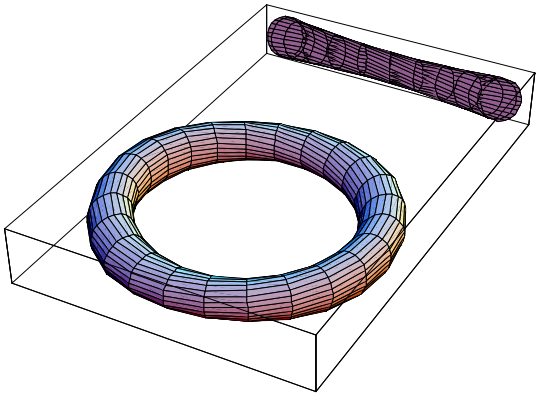

Mode 6 (24.85 Hz), h = 76.2 mm
3rd antisymmetric mode (twisting)

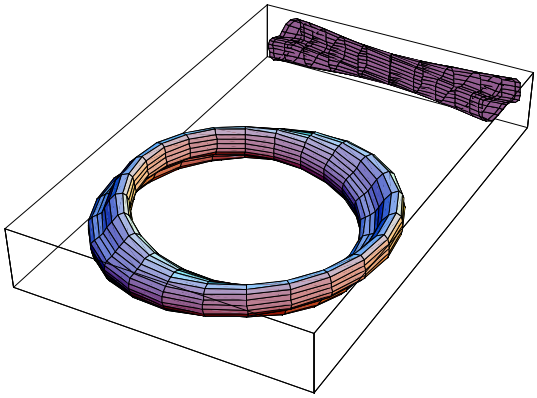

Mode 10 (11.96 Hz), h = 5 mm
3rd antisymmetric mode (twisting)

Fig. 4.11: Effect of the wall-thickness on the mode shapes.

4.7 Comparison of Different Shell Theories

A literature survey on the analysis of a shell under pressure suggests that there have been some variations in the way the effects of internal pressure have been handled. Differences in various approaches can be divided into two groups - one due to the approximations in geometric nonlinearity and the other due to neglecting the direct pressure force. While the former is linked to prestresses, the later is associated with the follower action of pressure. In Chapter 2, we noted that geometric nonlinearity is important to consider for coupling the prestresses with the equations of motion. Now, it matters how accurately the geometric nonlinearity is considered. We will see in this section that the differences in natural frequencies and mode shapes of an inflated torus arising from different theories necessitate the use of an accurate theory for such analyses. The inaccuracy due to the omission of the direct pressure force is a commonly followed practice in the analysis using commercial finite element codes. In the following subsections, we point out these effects (one at a time) and evidence in order to support the above-mentioned points.

4.7.1 Effects of Approximations in Geometric Nonlinearity

Here, we consider four strain-displacement relations, which were derived in Chapter 2 by simplifying Eqs. (2.36). The four different relations are summarized below:

1) Geometric nonlinearity (Eqs. 2.36) without any approximations related to the magnitudes of strains and displacements.

2) Sanders' nonlinear theory (Eqs. 2.105), which assumes that the linear in-plane membrane strains (ε_1^o, ε_2^o, ε_3^o, and ε_4^o) are much smaller than the rotations (β_1, β_2, and β_n) in nonlinearity.

3) The geometric relation used by Plaut et al. (2000), where, apart from the assumptions made in Sanders' nonlinear shell theory, the rotation (β_n) of the reference surface about

the normal is ignored compared to the rotations (β_1, β_2) of the tangents to the middle surface oriented along the coordinate lines.

4) Donnell's nonlinear theory (Eqs. 2.108), which, apart from the above assumptions, ignores the in-plane displacements (u_1, u_2) in comparison with the transverse displacement, w, in the nonlinear part of the strain-displacement relations. This theory was used by Saigal et al. (1986) for free vibration analysis of an inflated torus.

The natural frequencies and modes shapes calculated using the above four cases are then compared. In all these analyses, the pressure force will be kept in order to exclusively point out the effects of approximations in nonlinear terms.

Figure 4.12 compares the natural frequencies calculated using all the four cases. The four bars of a particular mode are arranged in the increasing order of approximation (Case (1) is most accurate and Case (4) is the least). A noticeable point in the figure is that the Sanders' shell theory gives almost the same result as obtained using Case (1). The results from the other two theories are not so accurate. The first frequency obtained using Case (3) is less than half of the frequency by Case (1). The other frequencies are also different but the differences are not so high. Moreover, the differences are higher in the lower frequencies. On the other hand, the first frequency corresponding to Donnell's nonlinearity, Case (4), is more than double of that from Case (1). Other frequencies corresponding to this theory are also significantly different, making it almost unusable in the present case. This idea is further reinforced by calculating the rigid-body-frequencies, which must be zero as the boundary conditions are free. Case (1) and Case (2) produce zero rigid-body frequencies. The theory corresponding to Case (3) gives zero frequencies corresponding to translation-type rigid-body modes and nonzero complex numbers corresponding to the rotation-type rigid-body modes. Case (4) produces rigid-body frequencies of the same order as the first non-rigid-body frequency calculated by the same theory. Moreover, all the rigid-body frequencies are non-zero.

The visible effect of these approximations on the mode shapes is that the order of modes changes. Table 4.6 lists the mode orders as given by different theories. The modes in each case are arranged in the increasing order of the corresponding frequencies. A particular entry of the table denotes which mode of Case (1) will occupy that position. For example, in Case (2), the third row entry is *4*. It means that if we arrange the mode shapes calculated using Case (2) in the increasing order of natural frequency, the third mode will be actually the fourth mode of Case (1). We see that the change in mode order occurs only in two locations in Cases (2) and (3), while there are several changes in Case (4). It again suggests that the performance of Case (4) is dismal.

From Fig. 4.12 and Table 4.6, one can infer that the rotation of the reference surface about the normal and the in-plane displacements are too important to ignore in the present case. It suggests that the consideration of an accurate geometric nonlinearity is very important for the case of an inflated torus and care must be taken in making any approximations.

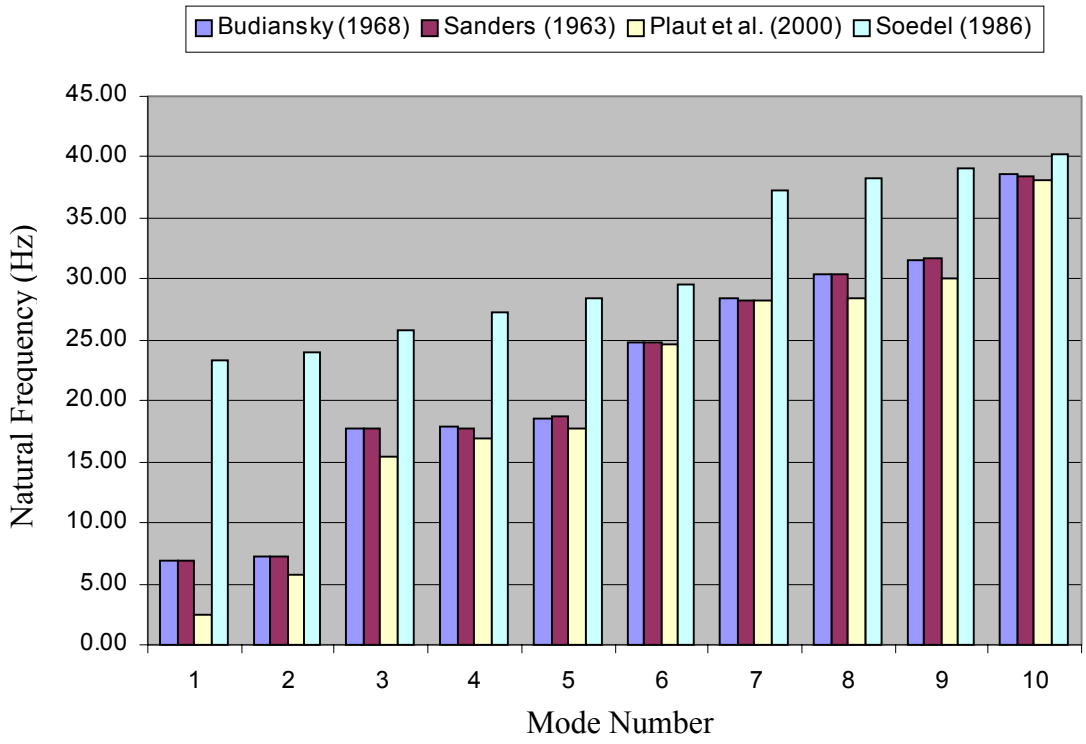

Fig. 4.12: Comparison of natural frequencies evaluated using different shell theories.

Table 4.6: Mode order of the first ten modes given by different theories.

Mode Number	Case (1)	Case (2)	Case (3)	Case (4)
1	1	1	1	**4**
2	2	2	2	**1**
3	3	**4**	3	**2**
4	4	**3**	**5**	**3**
5	5	5	**4**	**6**
6	6	6	6	**8**
7	7	7	7	**5**
8	8	8	8	**10**
9	9	9	9	**7**
10	10	10	10	**9**

Obviously, the effect of geometric nonlinearity will depend upon the internal pressure, wall-thickness, and the elastic modulus of the inflated torus. In other words, while this effect will be larger for higher internal pressure, it will be less for higher wall-thickness and elastic modulus, which make the torus stiffer. This makes it important to know how these parameters as a whole affect the natural frequencies. To this end, the first two natural frequencies are plotted against the prestress parameter, ζ (Eq. (4.29)). Figure 4.13 shows these plots for Case (1), Case (3), and Case (4). Case (2) was not included as it always gives frequencies close to those obtained using Case (1). As expected, all three analyses give the same frequencies at $\zeta = 0$, which corresponds to no initial stresses or infinitely stiff torus. However, as ζ grows, the results of Case (3) and Case (4) start deviating from the result of Case (1). The same phenomenon is noted regarding both the frequencies. Another fact that comes from these plots is that for $\zeta \leq 0.01$, results of Case (3) are much better compared to those of Case (4).

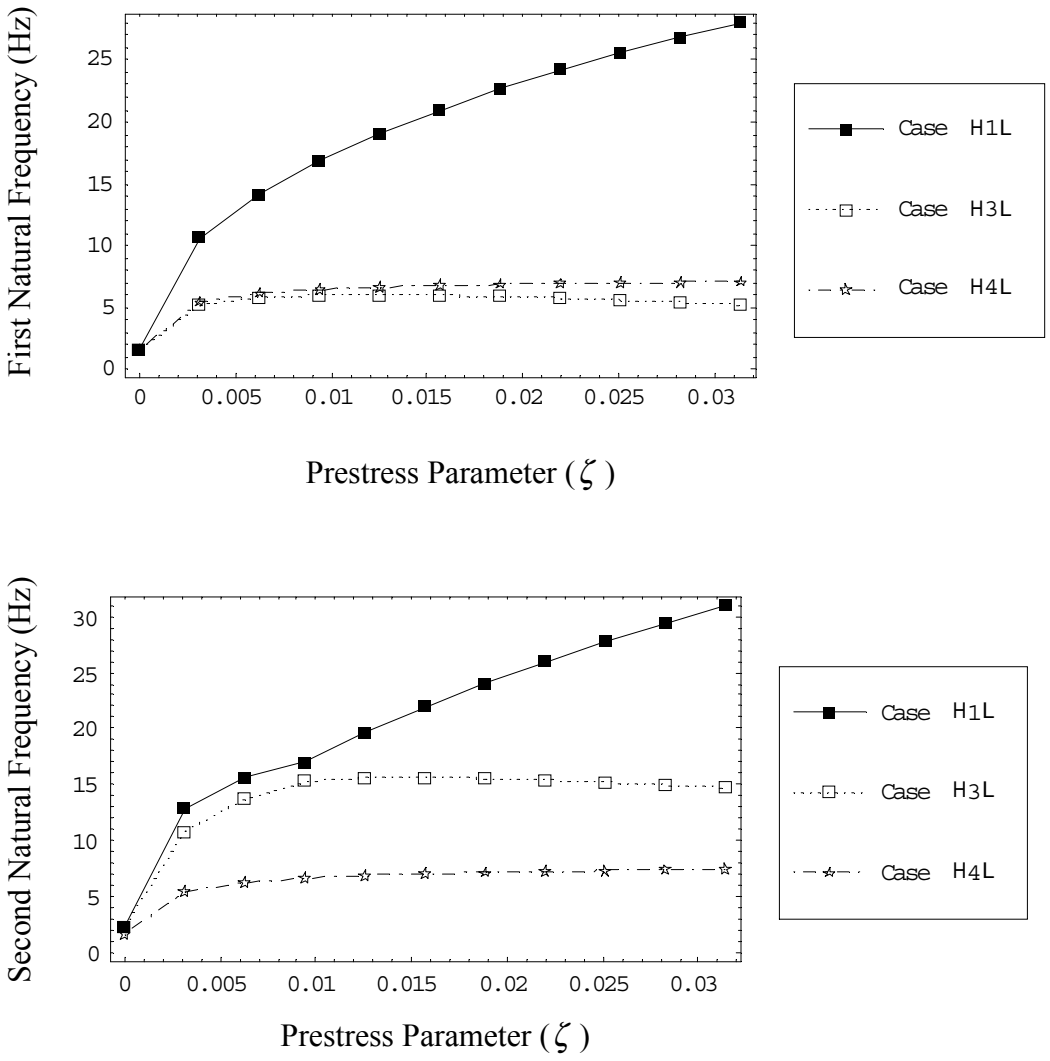

Fig. 4.13: Effect of prestress parameter on the natural frequencies as calculated using different geometric nonlinearities.

4.7.2 Effects of Pressure Force

As mentioned earlier, apart from producing initial stresses, internal pressure also exchanges energy due to its direct effect. This effect can be described using the so-called follower action of pressure force, where it is assumed that the pressure force always acts perpendicular to the surface of the shell while the shell is vibrating. Another modeling approach is to consider the pressure force as dead load, i.e., it does not change its direction

during shell vibration. In this section, we evaluate the effects of the follower action of pressure force (Eqs. (2.97)), which were ignored before (Saigal et al., 1986; Plaut et al., 2000; Lewis, 2001; Leigh et al., 2001). Figure 4.14 compares the natural frequencies calculated using the following three cases:

1) Considering the follower action of pressure force (Eqs. 2.97)
2) Ignoring the effect of pressure force
3) Finite element analysis (FEA) using ANSYS^{TM} (element type: Shell 93)

It can be seen from the figure that the first frequency from the finite element is analyzed around 25 % more than the frequency calculated using Case (1). Similarly, the second and the fifth frequencies are around 50 % higher. Also, the finite element analysis and Case (2) gives almost the same results. The result from the finite element analysis matches closely with that by Lewis (2001). One can conclude that the omission of pressure force, in effect, over-estimates the effective stiffness. This is why the frequency after neglecting the pressure is more than the actual one (except for the tenth mode). Similarly, Case (2) and Case (3) gives incorrect natural frequencies corresponding to the rigid-body modes of rotation type (Fig. 4.15). Compared to the translation-type rigid-body modes, the rotation-type is more critical, as the zero frequency criterion is more difficult to satisfy in this case. The effect of pressure force on the mode shapes is mostly on the mode order as shown in Table 4.7. For example, the first mode from FEA is actually the second mode calculated using Case (1). Another effect of excluding the pressure force is that the cross-sectional deformation of modes becomes higher (Table 4.8). This analysis suggests that the effect of pressure force is significant on the natural frequencies and mode shapes and should not be ignored.

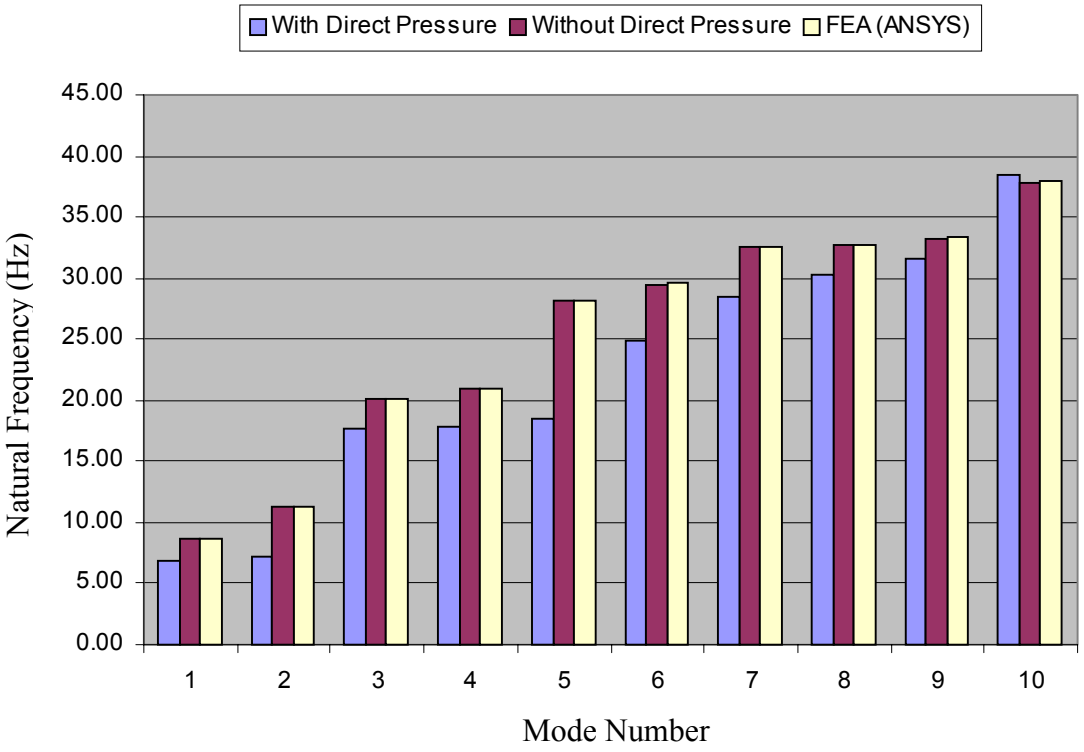

Fig. 4.14: Effect of the pressure force on the natural frequencies.

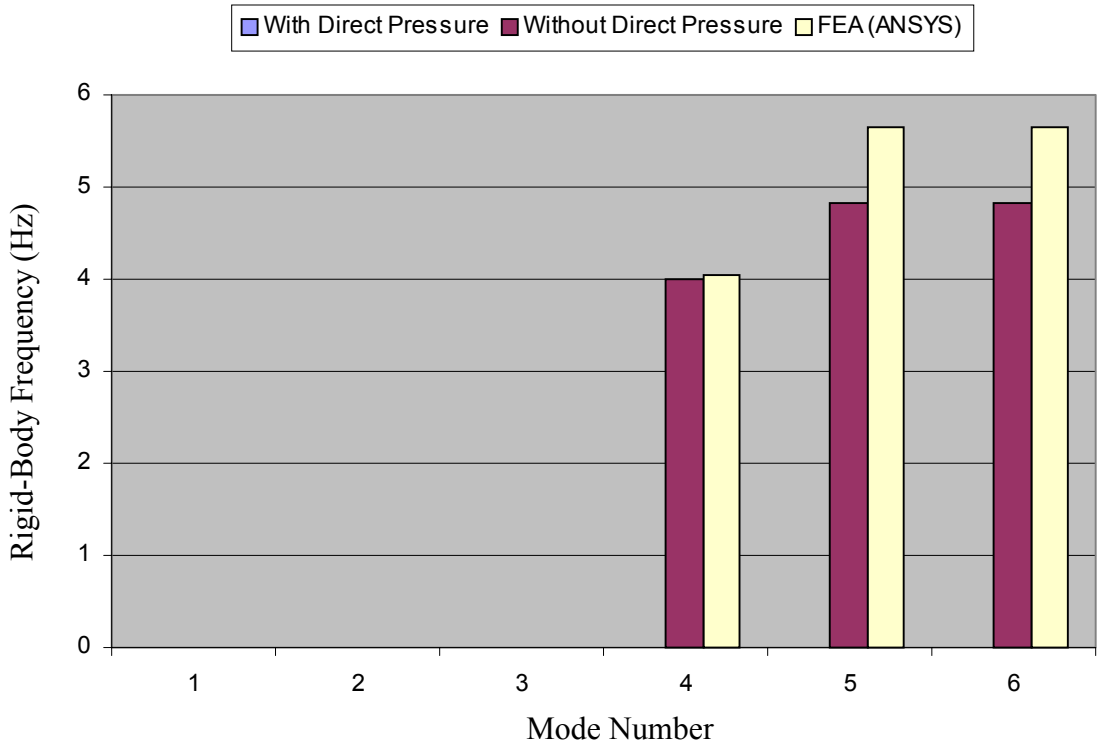

Fig. 4.15: Effect of the pressure force on the rigid-body frequencies.

Table 4.7: Comparison of mode orders with and without considering direct pressure.

Mode Number	With direct pressure effect	Without direct pressure effect
1	1	**2**
2	2	**1**
3	3	**5**
4	4	**3**
5	5	**7**
6	6	**4**
7	7	**8**
8	8	**9**
9	9	**6**
10	10	10

Table 4.8: Effect of pressure force on the deformation of modes.

With direct pressure effect	Without direct pressure effect
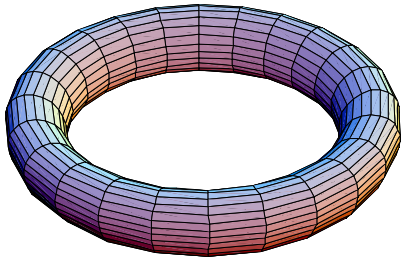 17.85 Hz, Mode number = 6, n = 0, Antisymmetric	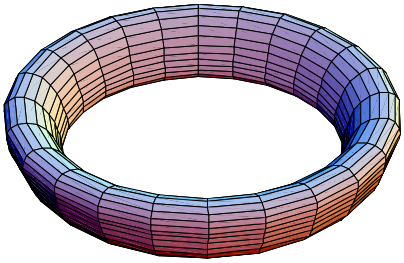 29.50 Hz, Mode number = 6, n = 0, Antisymmetric

4.8 Experimental Verification

Park, Ruggiero, and Inman (2002) performed experimental modal analysis using piezoelectric actuators and sensors, and presented the natural frequencies and mode shapes of an inflated torus. It is worth considering here how well the result of the present analysis matches with this experiment. Figure 4.16 shows the experimental torus. This torus is made by joining three 120^o segments with extended flaps on both sides. The joining region and the two flaps are shown in Fig. 4.17. Table 4.9 presents the values of its parameters. In order to simulate the free boundary condition, they hung the torus from a wall. Figure 4.18 compares the natural frequencies from the shell theory (Eqs. 2.97), FEA (ANSYS^{TM}), and experiment (Park, Ruggiero, and Inman, 2002). Clearly, the present shell theory gives better results when compared to the FEA because the pressure force has been included in the shell theory analysis. However, the result from the shell theory does not match exactly with the experiment. The reason could be that the present analysis does not account for the joining regions and flaps. These additional flaps and joining regions increase the mass of the inflated torus without bringing much change in its stiffness. Moreover, the experiments were not conducted in a vacuum condition. It has been shown in the past that the mass of air decreases the natural frequencies (Giraudeau, Pierron, and Chambard, 2002). Similarly, the influence of internal air was ignored in our study. This was, of course, present in the experiment, giving rise to an additional mass. The mass effect of the air is especially evident in a lightweight structure like the inflated torus. This is why the experiment shows lower frequencies than the shell analysis. Another reason could be the inaccuracy in simulating the free boundary condition in the experiment due to a small hanging wire. Park, Ruggiero, and Inman (2002) also presented the mode shapes of the inflated torus (Fig. 4.19). They presented only the in-plane and the out-of-plane bending modes but not other types of modes (e.g. axisymmetric mode, twisting modes, etc.). The in-plane and the out-of-plane bending mode shapes from the shell theory were found to be qualitatively the same as those obtained from the experiment. The symmetry and the wave number of the bending modes, shown in Fig 4.19, can be verified to be the same as those in Fig. 4.5. However the sequence of these modes did not agree with the result of ANSYS^{TM}.

Fig. 4.16: The inflated torus used in experiment (Park, Ruggiero, and Inman, 2002)

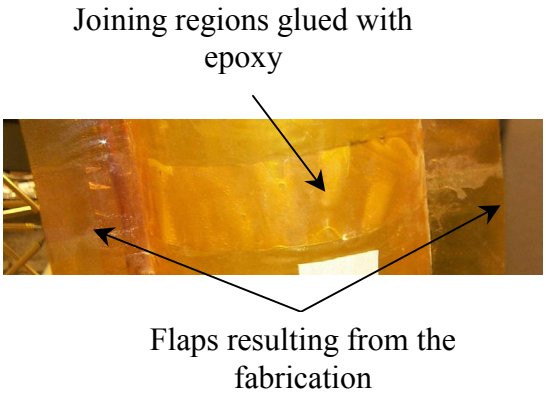

Fig. 4.17: Two flaps and a joining region.

Table 4.9: Data for the torus used in experiment.

Parameter	**Values**
Elastic modulus E, N/m^2	$2.55\mu 10^{9}$
Wall-thickness h, m	$46\ \mu 10^{-6}$
Poisson's ratio ν	0.34
Density ρ, Kg/m^3	1418
Radius of torus R, m	1.8
Radius of the cross-section r, m	0.15
Internal pressure p, N/m^2	3447.38
Joining region thickness, m	$300\ \mu 10^{-6}$
Joining region width, m	0.051

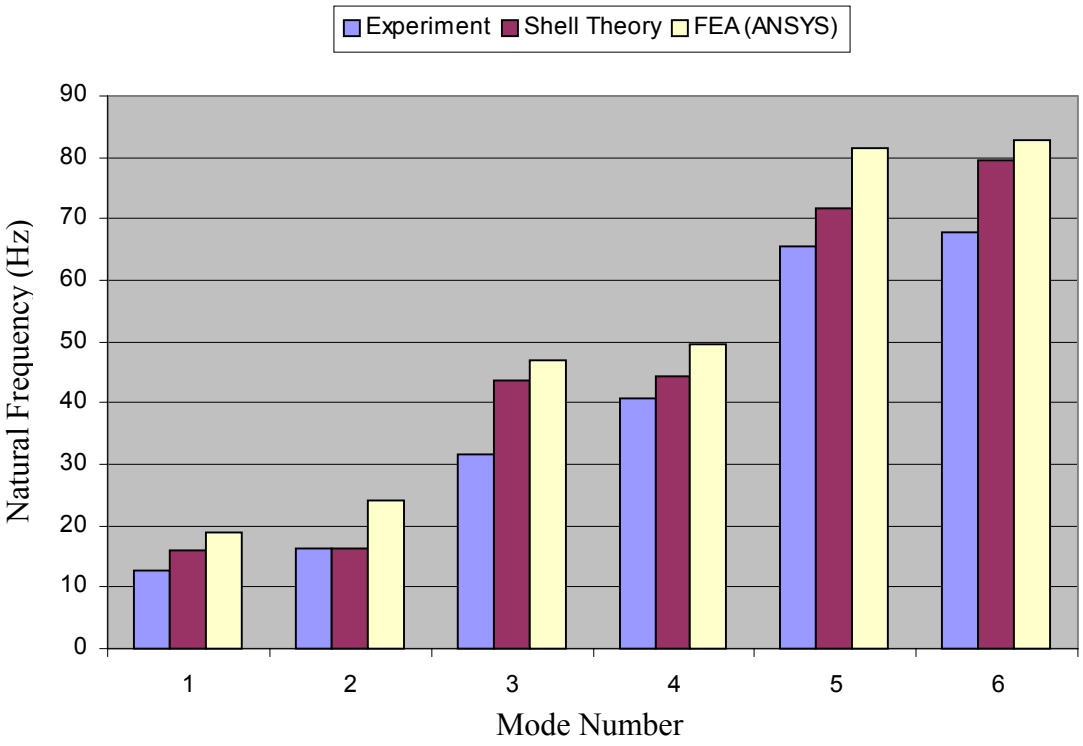

Fig. 4.18: Comparison of results from experiments, FEA (ANSYS^{TM}), and shell theory.

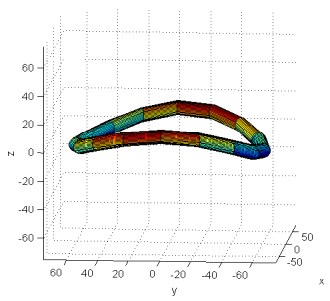

12.91 Hz, Mode 1
1st out-of-plane bending

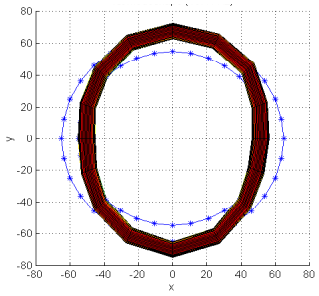

16.41 Hz, Mode 2
1st in-plane bending

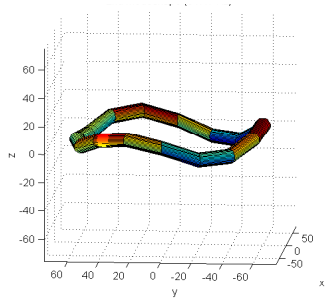

31.47 Hz, Mode 3
2nd out-of-plane bending

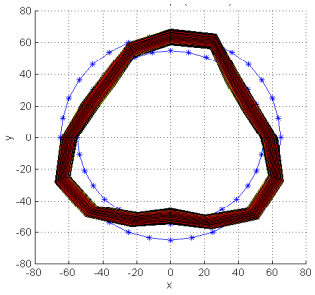

41.99 Hz, Mode 4
2nd in-plane bending

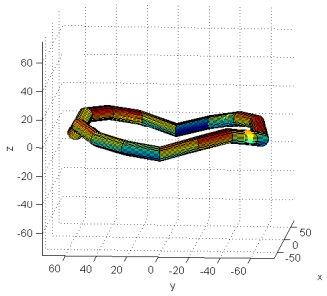

65.64 Hz, Mode 5
3rd out-of-plane bending

Fig. 4.19: Mode shapes obtained from experiment (Park, Ruggiero, and Inman, 2002)

4.9 Conclusions

The free vibration analysis of a complete inflated torus with circular cross-section and free boundary condition has been presented. The governing equations were formulated using Sanders' shell theory including geometric nonlinearity and the follower action of the pressure. In order to solve the partial differential equations, the displacement functions were represented in terms of sine and cosine waves in the longitudinal direction. This reduced the governing partial differential equations to a set of ordinary differential equations in the meridional coordinate ϕ, which was solved using Galerkin's method to obtain the mode shapes and the natural frequencies. The displacement functions in the ϕ-direction were written in two groups, called the symmetric and antisymmetric modes, using Fourier series.

First, we calculated the natural frequencies for a cylinder without pressure, which is a special case of an inflated torus. The results were found to match the exact solution. Then the case of an inflated torus was considered and the results were again compared with existing ones. The mode shapes and natural frequencies for both rigid-body and non-rigid-body modes were presented. It was observed that the analysis gives exactly zero frequencies for the rigid-body modes, which is consistent with the fact that the torus has free boundary conditions. In order to understand the effects of different parameters (aspect ratio, pressure, and thickness) on the vibration characteristics of the torus, parametric studies were performed. The natural frequencies were found to be mostly decreasing with the increase in the thickness and the aspect ratio. However, with the increase in pressure, the frequencies were found to be increasing. In all the three cases, the change was high initially and then it became slow. The effects of these parameters on the mode shapes were noted. In all the three cases, a change in mode order occurred with different parameter values. It was noticed that at low aspect ratio, the lower order modes mostly consist of ring-type modes. Effects of pressure and thickness were found to change the cross-sectional deformation.

Next, we evaluated the effects of geometric nonlinearity and the pressure force. In the case of the study related to geometric nonlinearity, we considered four different

approximations used in the past and compared the natural frequencies and mode shapes. We found that Sanders' nonlinear theory performs almost the same as the theory that does not make any assumption regarding the magnitudes of strains and rotation. It was found that the other two approximations are not so suitable and should be avoided for the present type of analysis. Similarly, the effect of pressure force should not be ignored. It is important to point out that some researchers used commercial finite element codes (ANSYS™, I-DEAS™, ABAQUS™) without realizing the fact that these codes, in general, do not include the effects of the pressure force, and hence produce incorrect natural frequencies and mode shapes for both rigid-body and non-rigid-body modes. These errors were pointed out in this study.

Finally, we compared the results with experimental data and found that the present analysis does fairly well compared to the finite element codes. The discrepancies in results could be attributed to imperfect torus and boundary conditions used in the experiment.